American Mineralogist, Volume 108, pages 738–743, 2023

Iron and aluminum substitution mechanism in the perovskite phase in the system $MgSiO_3$-$FeAlO_3$-MgO

Takayuki Ishii*[,1,2], Catherine McCammon[2,†], and Tomoo Katsura[2,‡]

[1]Center for High Pressure Science and Technology Advanced Research, Beijing, 100094, China
[2]Bayerisches Geoinstitut, University of Bayreuth, Universitätsstraße 30, 95447 Bayreuth, Germany

Abstract

Fe,Al-bearing $MgSiO_3$ perovskite (bridgmanite) is considered to be the most abundant mineral in Earth's lower mantle, hosting ferric iron in its structure as charge-coupled (Fe_2O_3 and $FeAlO_3$) and vacancy components ($MgFeO_{2.5}$ and $Fe_{2/3}SiO_3$). We examined concentrations of ferric iron and aluminum in the perovskite phase as a function of temperature (1700–2300 K) in the $MgSiO_3$-$FeAlO_3$-MgO system at 27 GPa using a multi-anvil high-pressure apparatus. We found a $LiNbO_3$-structured phase in the quenched run product, which was the perovskite phase under high pressures and high temperatures. The perovskite phase coexists with corundum and a phase with $(Mg,Fe^{3+},\square)(Al,Fe^{3+})_2O_4$ composition ($\square$ = vacancy). The $FeAlO_3$ component in the perovskite phase decreases from 69 to 65 mol% with increasing temperature. The Fe_2O_3 component in the perovskite phase remains unchanged at ~1 mol% with temperature. The *A*-site vacancy component of $Fe_{2/3}SiO_3$ in the perovskite phase exists as 1–2 mol% at 1700–2000 K, whereas 1 mol% of the oxygen vacancy component of $MgFeO_{2.5}$ appears at higher temperatures, although the analytical errors prevent definite conclusions. The *A*-site vacancy component might be more important than the oxygen vacancy component for the defect chemistry of bridgmanite in slabs and for average mantle conditions when the $FeAlO_3$ charge-coupled component is dominant.

Keywords: Bridgmanite, phase transition, multi-anvil press, high pressure, substitution mechanism, lower mantle

Introduction

$MgSiO_3$ perovskite (bridgmanite) is the most abundant phase in Earth's lower mantle and incorporates Al and Fe by substituting for Si and Mg. The flexible substitution in bridgmanite produces a wide range of compositional variations depending on pressure-temperature-composition conditions. Although the oxidation state in the lower mantle is considered to be below the iron-wüstite buffer (Frost and McCammon 2008), large amounts of ferric iron are expected in bridgmanite due to charge disproportionation of iron ($3\ FeO \rightarrow Fe_2O_3 + Fe$) when aluminum is present (Lauterbach et al. 2000; Frost et al. 2004; Irifune et al. 2010; Huang et al. 2021).

McCammon et al. (1997) reported an increased ferric iron content with increasing Al in pyroxene diamond inclusions with composition $(Mg,Fe,Al)(Si,Al)O_3$, considered to be derived from bridgmanite. Lauterbach et al. (2000) experimentally also found a positive correlation between Fe^{3+} and Al. These studies suggest that iron favors the ferric state in bridgmanite by mainly forming the $FeAlO_3$ charge-coupled component, making it a major component in bridgmanite.

The $FeAlO_3$ component can significantly affect the properties of bridgmanite. For example, incorporating $FeAlO_3$ decreases the bulk modulus and increases the density (e.g., Boffa Ballaran et al. 2012) and electrical conductivity (e.g., Yoshino et al. 2016). The $FeAlO_3$ component also affects Mg-Fe partitioning between bridgmanite and other lower-mantle ferromagnesian minerals in peridotite and basalt (e.g., Frost and Langenhorst 2002; Irifune et al. 2010). Thus, understanding the $FeAlO_3$ component in bridgmanite is essential to argue the structure and dynamics of the lower mantle.

There are other minor components in bridgmanite. Experiments in the ternary systems of MgO-SiO_2-Al_2O_3 and MgO-SiO_2-Fe_2O_3 demonstrated that the oxygen vacancy components such as $MgAlO_{2.5}$ and $MgFeO_{2.5}$ are included in bridgmanite (Navrotsky et al. 2003; Kojitani et al. 2007; Liu et al. 2017a; Fei et al. 2020; Ishii et al. 2022a). Oxygen vacancy-bearing bridgmanite should be more compressible than stoichiometric bridgmanite. In addition, an *A*-site vacancy component of $Fe^{3+}_{2/3}SiO_3$ has also been suggested, which should be compressible (Ismailova et al. 2016). The charge-coupled substitution components Al_2O_3 and Fe_2O_3 can also appear (Kubo and Akaogi 2000; Kojitani et al. 2007; Liu et al. 2017b; Fei et al. 2020). Although the Al and Fe^{3+} substitution mechanisms have been individually investigated in Fe- and Al-free systems, respectively, the substitution mechanisms of these components are still unclear in the Fe-, Al-bearing system.

Liu et al. (2020) investigated the chemistry of the perovskite phase in the $MgSiO_3$-$FeSiO_3$-Fe_2O_3-Al_2O_3 system at 27 GPa and 2000 K. They observed 65 mol% of $FeAlO_3$ with a few percent of the oxygen vacancy and *A*-site vacancy components of $MgFeO_{2.5}$ and $Fe_{2/3}SiO_3$, respectively, using samples with ferrous iron up to 25%. However, the temperature and pressure dependence of the chemistry of the perovskite phase in these systems is still unknown.

* E-mail: takayuki.ishii104@gmail.com. Orcid 0000-0002-1494-2141
† Orcid 0000-0001-5680-9106
‡ Orcid 0000-0001-7857-5101

0003-004X/23/0004–738$05.00/DOI: https://doi.org/10.2138/am-2022-8457

This study investigated the temperature dependence on the chemistry of the perovskite phase in the ferrous iron-free system MgO-$MgSiO_3$-$FeAlO_3$ at 27 GPa and 1700–2300 K using a multi-anvil apparatus. Excess MgO was added to explore the substitution mechanism in mantle assemblages with Mg/Si > 1, such as peridotite.

Experimental procedures

Starting material and high-pressure experiments

A mixture of $MgSiO_3$ enstatite, Mg_2SiO_4 forsterite, Al_2O_3 corundum, and Fe_2O_3 hematite with mole proportions of 5:20:37.5:37.5, respectively, was used as a starting material. By following Ishii et al. (2018a, 2019a), the enstatite and forsterite samples were synthesized by dissolving Mg metal in a solution of HNO_3 plus pure water, mixing it with tetraethylorthosilicate [$(CH_3CH_2O)_4Si$] at Mg/Si ratios of 1 and 2 for enstatite and forsterite, respectively, adding ammonia to the solutions, and heating the resulting gels stepwise to 1700 K. Reagent grades of Al_2O_3 and Fe_2O_3 were dried at 773 K for 24 h before weighing.

High pressure-high temperature syntheses were performed at 27 GPa and 1700, 2000, and 2300 K for 2–20 h using IRIS-15, a 15-MN Kawai-type multi-anvil press with an Osugi-type guide block system installed at the Bayerisches Geoinstitut, University of Bayreuth (Ishii et al. 2016, 2019b). The starting material was packed in a Pt-tube capsule, closed with two Pt lids. To avoid the reduction of Fe^{3+} to Fe^{2+}, which was observed by Liu et al. (2020), an IrO_2 oxidizer was also put at the bottom of the capsule, separating it from the sample using a Pt foil. A Cr-doped MgO octahedron with 7 mm edge lengths was used as a pressure medium. A cylindrical $LaCrO_3$ heater was inserted into the center of the octahedron. An MgO sleeve was placed in the heater to insulate the sample capsule from the heater electrically. Sample temperatures were measured at the surface of the capsule using a W97%Re3%–W75%Re25% thermocouple. The ceramic parts of the cell assemblies were kept at 1273 K for more than 3 h in an oven and taken out just before assembling them. The sample was always kept at 427 K in an oven and taken out just before assembling. The truncation size of the inner anvils was 3.0 mm. The sample was first compressed to 2 GPa (0.3 MN) at room temperature and heated to 600 K at a rate of 100 °C/min. These conditions were kept for 1~2 h to purge adhesive water in the sample and cell components. The assembly was then cooled to room temperature, compressed to 27 GPa (13 MN), and heated to the desired temperature at a rate of 100 °C/min. After keeping the target temperature, the sample was quenched by shutting off the electric power supply of the heater and slowly decompressed for 12–15 h.

To estimate a generated pressure of 27 GPa at 13 MN, we employed a pressure dependence of the alumina content in $MgSiO_3$ bridgmanite coexisting with corundum together with the decomposition pressure of pyrope to bridgmanite plus corundum (Hirose et al. 2001; Liu et al. 2017b) in separate runs. Pressure calibration has been generally performed using phase boundaries of compounds determined by in situ X-ray diffraction in a multi-anvil press. However, there is no such pressure calibrant to cover the present pressure range (>27 GPa) (Ito 2015). Hirose and Fei (2002) calibrated pressures to 27 GPa using Al_2O_3 content in bridgmanite reported by Hirose et al. (2001). Liu et al. (2017b) extended the pressure range to 52 GPa with more systematic data, and therefore the present calibration to estimate 27 GPa is most reliable for the time being. Our recent study reproduced 27.1(5) GPa at 13 MN using the same calibrant in the same multi-anvil press (Ishii et al. 2022b), supporting the validity of the present way.

Sample characterization

Phases in the recovered samples were identified using a micro-focused X-ray diffractometer (Bruker, D8 DISCOVER) operated at 40 kV and 500 μA equipped with a two-dimensional solid-state detector (VÅNTEC500) and a micro-focus source (IμS) of Co*K*α radiation. Phase compositions were measured using an electron microprobe analyzer (EPMA) with wavelength-dispersive spectrometers (JEOL, JXA-8200), operated at an accelerating voltage and probe current of 15 kV and 15 nA, respectively. The standards for Mg and Si, Al, and Fe were natural enstatite, synthetic corundum, and synthetic hematite, respectively. Sample textures were observed using a field-emission-type scanning electron microscope (SEM) (Zeiss LEO 1530 Gemini) with a detector for backscattered electron (BSE) imaging and an energy-dispersive X-ray spectrometer (Oxford X-Max^N).

Iron valence ratios in the recovered samples were determined by Mössbauer spectroscopy. The recovered samples were polished to 150 μm thickness. Mössbauer spectra were obtained at room temperature (293 K) in transmission mode on a constant acceleration Mössbauer spectrometer with a nominal 370 MBq ^{57}Co high specific activity source in a 12 μm thick Rh matrix (McCammon et al. 1991; McCammon 1994). The velocities in all spectra were calibrated using a reference spectrum of a 25 μm thick α-Fe foil certified by National Bureau of Standards (now referred to as the National Institute of Standards and Technology, standard reference material no. 1541) at room temperature. Spectra were collected for 1–2 days and fitted with the full transmission integral using MossA software (Prescher et al. 2012).

Results and Discussion

Tables 1 and 2 summarize experimental conditions, phases present, and chemical compositions of each sample. Figure 1 illustrates the room-temperature Mössbauer spectrum of the sample synthesized at 27 GPa and 2000 K. The hyperfine parameters for Mössbauer spectra of the bulk recovered samples obtained by fitting are also summarized in Table 1. Figures 2 and 3, respectively, show a representative X-ray diffraction (XRD) pattern and backscattered electron (BSE) images of the recovered samples. We applied heating durations of 2–20 h at 1700–2300 K, in which the sample annealed at 2300 K employed only 2 h (Table 1). Many phase-relation studies on multi-component systems such as pyrolite and basaltic crust compositions by multi-anvil press showed chemically homogeneous phases at 2000–2300 K even heated for 2 h or less (Ono et al. 2001; Hirose and Fei 2002; Ishii et al. 2011, 2012,

Table 1. Experimental conditions, phase assemblages, and chemical compositions of recovered bridgmanite

Run no.	I-1003	I-969	I-991
T (K)	1700	2000	2300
Heating duration (h)	20	13	2
Phases	LN+Crn+PS	LN+Crn+PS	LN+Crn+PS
n	8	9	12
Composition (wt%)			
MgO	9.44(37)	9.95(30)	10.91(38)
SiO_2	14.74(62)	15.62(50)	15.59(47)
Al_2O_3	29.05(58)	28.40(35)	27.18(61)
Fe_2O_3	47.61(82)	46.32(65)	45.21(73)
Total	100.85(130)	100.26(122)	98.89(148)
Composition (pfu) (O = 3)			
Mg	0.284(9)	0.300(6)	0.333(9)
Si	0.298(14)	0.315(8)	0.319(6)
Al	0.691(6)	0.676(5)	0.656(9)
Fe	0.723(8)	0.704(10)	0.697(12)
Cation total	1.996(7)	1.995(3)	2.005(4)
Mole fraction			
$MgSiO_3$	28(1)	30(1)	32(1)
$FeAlO_3$	69(1)	68(1)	65(1)
Fe_2O_3	1.2(9)	0.9(11)	1.3(18)
$Fe^{3+}_{2/3}SiO_3$	1.4(1.7)	1.6(10)	N
$MgFeO_{2.5}$	N	N	1.4(11)
$Fe^{3+}/\Sigma Fe$	100(5)	100(3)	100(5)
Hyperfine parameters			
CS for Fe^{3+}	0.33(1)	0.319(5)[a]	0.32(1)
QS for Fe^{3+}	0.92(2)	0.895(5)	0.92(2)
FWHM	0.48(4)	0.36(2)	0.47(4)

Notes: LN = $LiNbO_3$-type phase; Crn = corundum; PS = $A^{2+}B^{3+}_2O_4$ post-spinel phase; N = not observed; *n* = number of analyzed points; CS = center shift relative to α-Fe (mm/s); QS = quadrupole splitting (mm/s); FWHM = full-width at half maximum (mm/s). Numbers in parentheses for chemical composition data indicate one standard deviations of the mean in the analyses. Mole fractions of each component were calculated as follows (also see the text):

1. All Al is combined with corresponding amount of Fe^{3+} to form the $FeAlO_3$ component.
2. The *A*-site vacancy, corresponding to 1/3 of the *A*-site, is used to allocate Fe and Si to the $Fe^{3+}_{2/3}SiO_3$ component.
3. The O-vacancy corresponding to 0.5 of the $MgFe^{3+}O_{2.5}$ component forms the basis for the allocation of Fe and Mg.
4. The rest of Fe is allocated to the Fe_2O_3 component.
5. The rest of Mg and Si is allocated to the $MgSiO_3$ component.

[a] Broad, weak magnetic Fe^{3+} component with CS = 0.1(1) mm/s was also observed in the fitting (see Fig. 1).

Table 2. Chemical compositions of recovered post-spinel phases and corundum

Post-spinel phase, I-1003 (27 GPa, 1700 K), *n* = 9					
Oxide wt%	MgO	SiO_2	Al_2O_3	Fe_2O_3	Total
	21.32(31)	0.86(22)	29.93(52)	45.69(35)	97.81(46)
Cation number (O = 4)	Mg	Si	Al	Fe^{3+}	Total
	0.921(13)	0.025(6)	1.022(15)	0.996(10)	2.965(5)
Post-spinel phase, I-969 (27 GPa, 2000 K), *n* = 8					
Oxide wt%	MgO	SiO_2	Al_2O_3	Fe_2O_3	Total
	22.73(38)	0.75(4)	30.39(60)	45.05(48)	98.93(73)
Cation number (O = 4)	Mg	Si	Al	Fe^{3+}	Cation
	0.968(9)	0.022(1)	1.024(14)	0.969(15)	2.982(3)
Corundum, I-969 (27 GPa, 2000 K), *n* = 6					
Oxide wt%	MgO	SiO_2	Al_2O_3	Fe_2O_3	Total
	4.20(10)	6.19(27)	73.84(56)	14.80(56)	99.03(65)
Cation number (O = 3)	Mg	Si	Al	Fe^{3+}	Cation
	0.113(3)	0.112(5)	1.574(12)	0.201(7)	2.000(1)
Post-spinel phase, I-991 (27 GPa, 2300 K), *n* = 8					
Oxide wt%	MgO	SiO_2	Al_2O_3	Fe_2O_3	Total
	21.19(18)	1.64(9)	30.44(41)	44.48(41)	97.75(55)
Cation number (O = 4)	Mg	Si	Al	Fe^{3+}	Cation
	0.910(1)	0.047(2)	1.033(11)	0.964(5)	2.954(3)
Corundum, I-991 (27 GPa, 2300 K), *n* = 6					
Oxide wt%	MgO	SiO_2	Al_2O_3	Fe_2O_3	Total
	3.73(4)	5.24(17)	74.27(77)	14.49(32)	97.72(92)
Cation number (O = 3)	Mg	Si	Al	Fe^{3+}	Cation
	0.102(1)	0.096(3)	1.604(4)	0.200(3)	2.002(1)

Note: *n* = number of analyzed points. Numbers in parentheses indicate one standard deviations of the mean in the analyses.

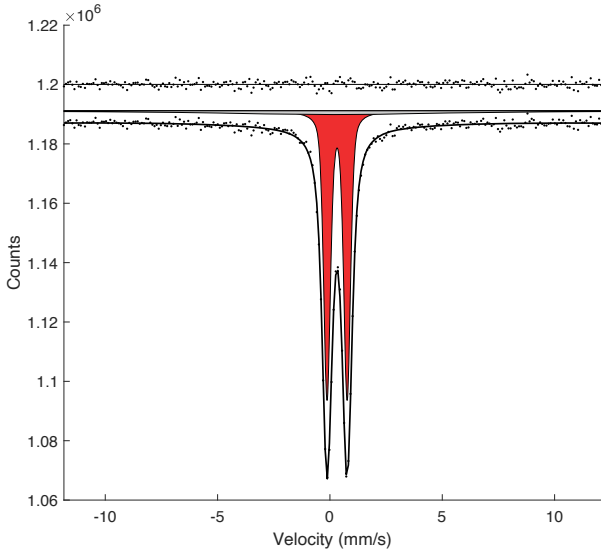

Figure 1. Room-temperature Mössbauer spectrum of the recovered sample synthesized at 27 GPa and 2000 K. The red-shaded area is assigned to non-magnetic Fe^{3+}. The gray shaded area is assigned to weakly magnetic Fe^{3+}. Spectra of samples quenched from 1700 and 2300 K contain only non-magnetic Fe^{3+}. (Color online.)

2018b, 2019c, 2022b). In fact, the well-crystallized texture and homogeneous chemical compositions of the recovered phases (Tables 1 and 2; Fig. 3) suggest reaching equilibrium in the present heating durations at the pressure-temperature conditions used.

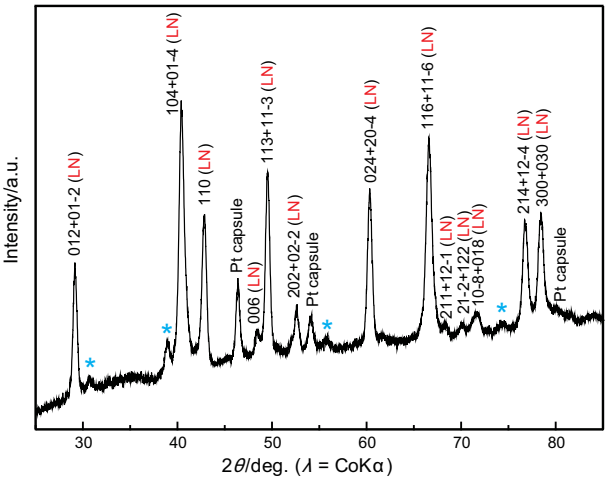

Figure 2. X-ray diffraction pattern of the recovered sample synthesized at 27 GPa and 2000 K. Stars indicate possible peaks of $(Mg,Al,Fe^{3+})O_4$ post-spinel phase (see text). LN = lithium niobate phase. (Color online.)

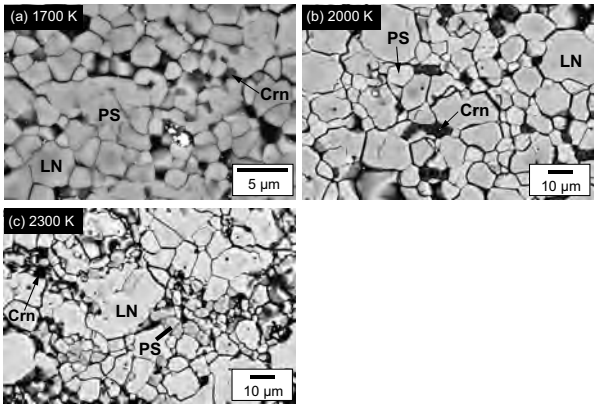

Figure 3. Backscattered electron images of recovered samples at 27 GPa and 1700–2300 K. White grains are platinum from the platinum capsule after polishing. LN = lithium niobate phase; Crn = corundum; PS = $(Mg,Al,Fe^{3+})O_4$ post-spinel phase.

Ferric iron contents

Mössbauer spectra of the bulk recovered samples can be fitted to one doublet, although one broad peak was also detected only on sample I-969 (Fig. 1). The hyperfine parameters of the center shift and quadrupole splitting are 0.32–0.33 mm/s and 0.90–0.93 mm/s, respectively, which are in good agreement with those of Fe^{3+} in bridgmanite and the $LiNbO_3$-structured phases (Fei et al. 1994; McCammon et al. 2004; Hummer and Fei 2012; Liu et al. 2020; Huang et al. 2021). The broad peak of sample I-969 can be assigned to a weakly magnetic Fe^{3+} component. All observed peaks were thus assigned to Fe^{3+}, showing $Fe^{3+}/\Sigma Fe$ = 100% in all samples.

Phase identification

Most XRD peaks were assigned to a $LiNbO_3$-structured phase (Fig. 2), known as a back-transformed phase from a

perovskite phase (Leinenweber et al. 1991; Akaogi et al. 2017; Ishii et al. 2017a; Liu et al. 2020). Liu et al. (2020) reported that the $MgSiO_3$-bearing perovskite phase with more than 40% of $FeAlO_3$ was recovered as a lithium-niobate phase at ambient conditions. Therefore, the chemistry of the $LiNbO_3$-structured phase should represent that of the perovskite-structured phase under high pressure-temperature conditions. Hereafter, we refer to this phase as the perovskite phase when discussing the crystal chemistry at high pressure and high temperature.

The BSE images showed three phases with different textures and contrasts in addition to the $LiNbO_3$-structured phase. One is a Mg,Al,Fe-rich phase with grain-crack texture. Its main components are $MgAl_2O_4$ and $MgFe_2O_4$, implying that this phase may be one of the $A^{2+}B_2^{3+}O_4$ orthorhombic phases, so-called post-spinel (PS) phases, which have an octahedral framework and a trigonal prism site (Ishii et al. 2018c). These phases are difficult to identify because they have similar crystal structures but different atomic distributions (Ishii et al. 2020). The XRD peaks not belonging to the $LiNbO_3$-structured phase can be assigned to a PS phase (Fig. 2). However, the XRD patterns do not clearly indicate which PS phase produces the few observed peaks. Nevertheless, these peaks can be assigned to the $CaTi_2O_4$-type phase, which was recently discovered in various AB_2O_4 compositions (Funamori et al. 1998; Bindi et al. 2014; Ishii et al. 2014, 2015, 2021). We refer to this phase as a PS phase hereafter. The BSE images also indicate limited amounts (~1.5–3 vol%) of an Al-rich phase, which was identified as corundum because this phase can be regarded as an Al_2O_3-$MgSiO_3$-Fe_2O_3 solid solution. However, XRD patterns indicated no corundum peaks, probably due to the limited intensities. The detailed compositions of these phases are discussed below.

Compositions of the perovskite phase

The component fractions in the $ABO_{3\pm\delta}$ perovskite phase were estimated using EPMA and Mössbauer data based on the following assumptions: (1) Al and Fe^{3+} produce the most charge-coupled component of $FeAlO_3$. The remaining trivalent cations are referred to as *T*. (2) When the cation-oxygen ratio is smaller than 2:3, the *A*-site cation-vacancy component $T_{2/3}SiO_3$ is considered. When greater, the oxygen vacancy component $MgTO_{2.5}$ is considered. (3) The remaining *T* produces the charge-coupled component TTO_3. (4) The remaining Mg^{2+} and Si^{4+} produce the $MgSiO_3$ component.

Figure 4 shows the changes in components of the perovskite phase with temperature obtained by the above procedure. Fe^{3+} and Al^{3+} ions dominate, resulting in the dominant component $FeAlO_3$. This component slightly decreases with increasing temperature from 69 to 65 mol%. The second major component is $MgSiO_3$, which increases with increasing temperature from 28 to 32 mol%. Thus, the perovskite phase in the present system can be approximated by a $MgSiO_3$-$FeAlO_3$ solid solution. Liu et al. (2020) reported that the perovskite phase synthesized at 27 GPa and 2000 K in the $MgSiO_3$-$FeSiO_3$-Fe_2O_3-Al_2O_3 system without excess MgO has 63–65 mol% of the $FeAlO_3$ component. These values are slightly smaller than the present study (67 mol% at 2000 K), probably because Fe^{3+} in their perovskite phase (11–15%) was slightly reduced to Fe^{2+} to form some $Fe^{2+}SiO_3$ components. We observed 1~2 mol% of the *A*-site vacancy component of $Fe_{2/3}^{3+}SiO_3$ at lower temperatures of 1700 and 2000 K, whereas 1 mol% of the oxygen vacancy component $MgFeO_{2.5}$ was found at 2300 K. Although this change is within the analytical errors, the dominant vacancy component might change with temperature. In addition, we observed small amounts, only 1 mol%, of the charge-coupled component Fe_2O_3 in all perovskite phases, which showed no temperature dependence.

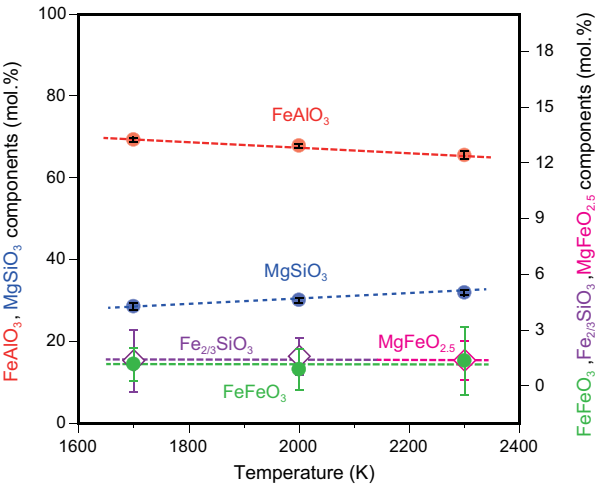

FIGURE 4. Solubility of $MgSiO_3$, $FeAlO_3$, Fe_2O_3, $Fe_{2/3}SiO_3$, and $MgFeO_{2.5}$ components in the perovskite-structured phase at 27 GPa as a function of temperature. (Color online.)

Compositions of the associated phases

As mentioned above, we found two phases associated with the $LiNbO_3$-structured phase, i.e., the PS phase and corundum. The primary composition of the PS phase can be expressed as $MgAl_2O_4$-$MgFe_2O_4$. However, there are extra ferric irons. Such extra Fe^{3+} should produce an *A*-site vacancy component $Fe_{2/3}Fe_2O_4$ because the total cation number is <3 for four oxygen atoms. This component is the third most abundant, representing 5–13 mol% of the phase. This phase also has a minor component of Mg_2SiO_4 (2–5 mol%) because of the small amounts of SiO_2 (0.8–1.6 wt%). The limited Si contents are typical in PS-related oxides, supporting the phase identification as a PS phase (Ishii et al. 2017b, 2018d; Akaogi et al. 2018; Uenver-Thiele et al. 2018). Thus, the compositions of the PS phase can be expressed as $(Mg,Fe^{3+},\square)(Al,Fe)_2O_4$ ($\square$ = vacancy), and is almost independent of the temperature.

The composition of corundum is expressed as Al_2O_3-$MgSiO_3$-Fe_2O_3, as mentioned above. There appears to be almost no temperature dependence, although composition at 1700 K is unknown due to the exceedingly small grain sizes (≲~1 μm) for EPMA analysis. The Al_2O_3, $MgSiO_3$, and Fe_2O_3 contents are 80, 10, and 10 mol%, respectively.

Reaction controlling the chemistry of the perovskite phase

The present system essentially has four chemical components: MgO, Fe_2O_3, Al_2O_3, and SiO_2. On the other hand, the number of phases is three: perovskite phase, an $A^{2+}B_2^{3+}O_4$ PS phase, and corundum. Therefore, the present system has one degree of freedom at a given pressure and temperature, which would be the partitioning of the $FeAlO_3$ charge-coupled component because Al_2O_3 and Fe_2O_3 are strongly coupled in the perovskite phase in the present system.

The resulting equilibrium reaction may be:

$$FeAlO_3 \text{ (perovskite phase)} + Mg_2SiO_4 \text{ (PS)} = MgFeAlO_4 \text{ (PS)} + MgSiO_3 \text{ (perovskite phase)} \quad (1)$$

The coincident decrease and increase in $FeAlO_3$ and $MgSiO_3$ components, respectively, with temperature (Fig. 4) suggest that the entropy change with this reaction is slightly positive.

Implications

The oxygen-vacancy components $MgAlO_{2.5}$ and $MgFeO_{2.5}$ have been proposed to exist in bridgmanite in the systems MgO-SiO_2-Al_2O_3 and MgO-SiO_2-Fe_2O_3, respectively (Liu et al. 2017a; Fei et al. 2020). The oxygen vacancy components should increase compressibility. Also, they possibly reduce the creep strength of bridgmanite, suggesting a viscosity contrast compared with the mantle containing stoichiometric bridgmanite (Liu et al. 2017a; Reali et al. 2019). Our study demonstrates that the vacancy component changes from *A*-site cation vacancy to oxygen vacancy with increasing temperature. Thus, the oxygen vacancy components are expected to be present in high-temperature regions such as plumes (White and McKenzie 1995). On the other hand, our results also suggest that the *A*-site cation vacancy should be more stable in relatively low-temperature regions such as subducted slabs.

These vacancy components should dominate in shallower regions of the lower mantle, namely the mid-mantle, due to their low density (Liu et al. 2017a). Although the proportions of vacancy components are small, percent-order vacancies should be enough to soften mineral strength (Reali et al. 2019). Therefore, the vacancy components would soften the mid-mantle to enhance mantle dynamics and geochemical circulation. Slab penetration and stagnation in the mid-mantle (Fukao and Obayashi 2013) and plumes becoming invisible by seismic tomography (French and Romanowicz 2015) may reflect the lower viscosity of the mid-mantle compared to deeper regions.

Vacancy in bridgmanite may also play an important role in incorporating water as OH groups in its crystal structure, which has significant importance for the geochemical evolution of the mantle. The oxygen vacancy component of $MgAlO_{2.5}$ may accommodate water based on the following reaction: $MgAlO_{2.5} + ½H_2O \rightarrow MgAlHO_3$ (e.g., Navrotsky 1999). The oxygen vacancy component of $MgFe^{3+}O_{2.5}$ would allow the incorporation of water in the same manner. The *A*-site vacancy component of $Fe^{3+}_{2/3}SiO_3$ might also have the capability to include water based on the following reaction: $Fe^{3+}_{2/3}SiO_3 + 1/3H_2O \rightarrow Fe^{3+}_{2/3}(OH)_{1/3}SiO_3H_{1/3}$. Thus, both vacancy components may be potential hosts for water in the lower mantle.

However, the pressure dependence of the vacancy components has not been investigated. Such a study requires a wide pressure range, which is impossible using conventional multi-anvil technology. On the other hand, no percent-order vacancy components can be detected by diamond anvil experiments due to relatively large chemical heterogeneity. Therefore, future experiments will focus on exploring the pressure dependence of vacancy concentrations to provide better constraints on their influence on lower mantle dynamics. Our ultrahigh-pressure multi-anvil technology (Ishii et al. 2016, 2017c, 2019b, 2022b) provides the best possibility to investigate pressure dependence, and we will tackle this task in the next study.

Acknowledgments and Funding

We thank H. Fischer and R. Njul for the preparation of cell assemblies and thin-section samples for Mössbauer measurements, respectively. We are also grateful to R.G. Tronnes and O. Müntener for their constructive comments. We thank two anonymous reviewers for their fruitful comments. This work was funded by research projects approved by the European Research Council (ERC) under the European Union's Horizon 2020 research and innovation programme (Proposal No. 787 527) to T. Katsura and the German Research Foundation (DFG) grant (IS350/1-1) to T. Ishii. The NSFC National Key Research Major Research Plan on West-Pacific Earth System Multispheric Interactions (grant 92158206 to T. Ishii.) also supported this work.

References cited

Akaogi, M., Abe, K., Yusa, H., Ishii, T., Tajima, T., Kojitani, H., Mori, D., and Inaguma, Y. (2017) High-pressure high-temperature phase relations in $FeTiO_3$ up to 35 GPa and 1600 °C. Physics and Chemistry of Minerals, 44, 63–73, https://doi.org/10.1007/s00269-016-0836-3.

Akaogi, M., Kawahara, A., Kojitani, H., Yoshida, K., Anegawa, Y., and Ishii, T. (2018) High-pressure phase transitions in $MgCr_2O_4$·Mg_2SiO_4 composition: Reactions between olivine and chromite with implications for ultrahigh-pressure chromitites. American Mineralogist. American Mineralogist, 103, 161–170, https://doi.org/10.2138/am-2018-6135.

Boffa Ballaran, T., Kurnosov, A., Glazyrin, K., Frost, D.J., Merlini, M., Hanfland, M., and Caracas, R. (2012) Effect of chemistry on the compressibility of silicate perovskite in the lower mantle. Earth and Planetary Science Letters, 333–334, 181–190, https://doi.org/10.1016/j.epsl.2012.03.029.

Bindi, L., Sirotkina, E., Bobrov, A.V., and Irifune, T. (2014) X-ray single-crystal structural characterization of $MgCr_2O_4$, a post-spinel phase synthesized at 23 GPa and 1600° C. Journal of Physics and Chemistry of Solids, 75, 638–641, https://doi.org/10.1016/j.jpcs.2014.01.008.

Fei, Y., Virgo, D., Mysen, B.O., Wang, Y., and Mao, H.K. (1994) Temperature-dependent electron delocalization in $(Mg,Fe)SiO_3$ perovskite. American Mineralogist, 79, 826–837.

Fei, H., Liu, Z., McCammon, C., and Katsura, T. (2020) Oxygen vacancy substitution linked to ferric iron in bridgmanite at 27 GPa. Geophysical Research Letters, 47(6), e2019GL086296.

French, S.W. and Romanowicz, B. (2015) Broad plumes rooted at the base of the Earth's mantle beneath major hotspots. Nature, 525, 95–99, https://doi.org/10.1038/nature14876.

Frost, D.J. and Langenhorst, F. (2002) The effect of Al_2O_3 on Fe-Mg partitioning between magnesiowüstite and magnesium silicate perovskite. Earth and Planetary Science Letters, 199, 227–241, https://doi.org/10.1016/S0012-821X(02)00558-7.

Frost, D.J. and McCammon, C.A. (2008) The redox state of Earth's mantle. Annual Review of Earth and Planetary Sciences, 36, 389–420, https://doi.org/10.1146/annurev.earth.36.031207.124322.

Frost, D.J., Liebske, C., Langenhorst, F., McCammon, C.A., Trønnes, R.G., and Rubie, D.C. (2004) Experimental evidence for the existence of iron-rich metal in the Earth's lower mantle. Nature, 428, 409–412, https://doi.org/10.1038/nature02413.

Fukao, Y. and Obayashi, M. (2013) Subducted slabs stagnant above, penetrating through, and trapped below the 660 km discontinuity. Journal of Geophysical Research. Solid Earth, 118, 5920–5938, https://doi.org/10.1002/2013JB010466.

Funamori, N., Jeanloz, R., Nguyen, J.H., Kavner, A., Caldwell, W.A., Fujino, K., Miyajima, N., Shinmei, T., and Tomioka, N. (1998) High-pressure transformations in $MgAl_2O_4$. Journal of Geophysical Research, 103, (B9), 20813–20818, https://doi.org/10.1029/98JB01575.

Hirose, K. and Fei, Y. (2002) Subsolidus and melting phase relations of basaltic composition in the uppermostlower mantle. Geochimica et Cosmochimica Acta, 66, 2099–2108, https://doi.org/10.1016/S0016-7037(02)00847-5.

Hirose, K., Fei, Y., Ono, S., Yagi, T., and Funakoshi, K. (2001) In situ measurements of the phase transition boundary in $Mg_3Al_2Si_3O_{12}$: Implications for the nature of the seismic discontinuities in the Earth's mantle. Earth and Planetary Science Letters, 184, 567–573, https://doi.org/10.1016/S0012-821X(00)00354-X.

Huang, R., Boffa Ballaran, T., McCammon, C.A., Miyajima, N., Dolejš, D., and Frost, D.J. (2021) The composition and redox state of bridgmanite in the lower mantle as a function of oxygen fugacity. Geochimica et Cosmochimica Acta, 303, 110–136, https://doi.org/10.1016/j.gca.2021.02.036.

Hummer, D.R. and Fei, Y. (2012) Synthesis and crystal chemistry of Fe^{3+}-bearing $(Mg,Fe^{3+})(Si,Fe^{3+})$ O_3 perovskite. American Mineralogist, 97, 1915–1921, https://doi.org/10.2138/am.2012.4144.

Irifune, T., Shinmei, T., McCammon, C.A., Miyajima, N., Rubie, D.C., and Frost, D.J. (2010) Iron partitioning and density changes of pyrolite in Earth's lower mantle. Science, 327, 193–195, https://doi.org/10.1126/science.1181443.

Ishii, T., Kojitani, H., and Akaogi, M. (2011) Post-spinel transitions in pyrolite and Mg_2SiO_4 and akimotoite-perovskite transition in $MgSiO_3$: Precise comparison by

high-pressure high-temperature experiments with multi-sample cell technique. Earth and Planetary Science Letters, 309, 185–197, https://doi.org/10.1016/j.epsl.2011.06.023.

——— (2012) High-pressure phase transitions and subduction behavior of continental crust at pressure–temperature conditions up to the upper part of the lower mantle. Earth and Planetary Science Letters, 357–358, 31–41, https://doi.org/10.1016/j.epsl.2012.09.019.

Ishii, T., Kojitani, H., Tsukamoto, S., Fujino, K., Mori, D., Inaguma, Y., Tsujino, N., Yoshino, T., Yamazaki, D., Higo, Y., and others. (2014) High-pressure phase transitions in $FeCr_2O_4$ and structure analysis of new post-spinel $FeCr_2O_4$ and $Fe_2Cr_2O_5$ phases with meteoritical and petrological implications. American Mineralogist, 99, 1788–1797, https://doi.org/10.2138/am.2014.4736.

Ishii, T., Kojitani, H., Fujino, K., Yusa, H., Mori, D., Inaguma, Y., Matsushita, Y., Yamaura, K., and Akaogi, M. (2015) High-pressure high-temperature transitions in $MgCr_2O_4$ and crystal structures of new post-spinel $MgCr_2O_4$ and $Mg_2Cr_2O_5$ phases. American Mineralogist, 100, 59–65, https://doi.org/10.2138/am-2015-4818.

Ishii, T., Shi, L., Huang, R., Tsujino, N., Druzhbin, D., Myhill, R., Li, Y., Wang, L., Yamamoto, T., Miyajima, N., and others. (2016) Generation of pressures over 40 GPa using Kawai-type multi-anvil press with tungsten carbide anvils. The Review of Scientific Instruments, 87, 024501, https://doi.org/10.1063/1.4941716.

Ishii, T., Sinmyo, R., Komabayashi, T., Boffa Ballaran, T., Kawazoe, T., Miyajima, N., Hirose, K., and Katsura, T. (2017a) Synthesis and crystal structure of $LiNbO_3$-type $Mg_3Al_2Si_3O_{12}$: A possible indicator of shock conditions of meteorites. American Mineralogist. American Mineralogist, 102, 1947–1952, https://doi.org/10.2138/am-2017-6027.

Ishii, T., Tsujino, N., Arii, H., Fujino, K., Miyajima, N., Kojitani, H., Kunimoto, T., and Akaogi, M. (2017b) A shallow origin of so-called ultrahigh-pressure chromitites, based on single-crystal X-ray structure analysis of the high-pressure $Mg_2Cr_2O_5$ phase, with modified ludwigite-type structure. American Mineralogist. American Mineralogist, 102, 2113–2118, https://doi.org/10.2138/am-2017-6050.

Ishii, T., Yamazaki, D., Tsujino, N., Xu, F., Liu, Z., Kawazoe, T., Yamamoto, T., Druzhbin, D., Wang, L., Higo, Y., and others. (2017c) Pressure generation to 65 GPa in a Kawai-type multi-anvil apparatus with tungsten carbide anvils. High Pressure Research, 37, 507–515, https://doi.org/10.1080/08957959.2017.1375491.

Ishii, T., Huang, R., Fei, H., Koemets, I., Liu, Z., Maeda, F., Yuan, L., Wang, L., Druzhbin, D., Yamamoto, T., and others. (2018a) Complete agreement of the post-spinel transition with the 660-km seismic discontinuity. Scientific Reports, 8, 6358, https://doi.org/10.1038/s41598-018-24832-y.

Ishii, T., Kojitani, H., and Akaogi, M. (2018b) Phase relations and mineral chemistry in pyrolitic mantle at 1600–2200° C under pressures up to the uppermost lower mantle: Phase transitions around the 660-km discontinuity and dynamics of upwelling hot plumes. Physics of the Earth and Planetary Interiors, 274, 127–137, https://doi.org/10.1016/j.pepi.2017.10.005.

Ishii, T., Sakai, T., Kojitani, H., Mori, D., Inaguma, Y., Matsushita, Y., Yamaura, K., and Akaogi, M. (2018c) High-pressure phase relations and crystal structures of postspinel phases in MgV_2O_4, FeV_2O_4, and $MnCr_2O_4$: Crystal chemistry of AB_2O_4 postspinel compounds. Inorganic Chemistry, 57, 6648–6657, https://doi.org/10.1021/acs.inorgchem.8b00810.

Ishii, T., Uenver-Thiele, L., Woodland, A.B., Alig, E., and Boffa Ballaran, T. (2018d) Synthesis and crystal structure of Mg-bearing Fe_9O_{11}: New insight in the complexity of Fe-Mg oxides at conditions of the deep upper mantle. American Mineralogist. Journal of Earth and Planetary Materials, 103, 1873–1876.

Ishii, T., Huang, R., Myhill, R., Fei, H., Koemets, I., Liu, Z., Maeda, F., Yuan, L., Wang, L., Druzhbin, D., and others. (2019a) Sharp 660-km discontinuity controlled by extremely narrow binary post-spinel transition. Nature Geoscience, 12, 869–872, https://doi.org/10.1038/s41561-019-0452-1.

Ishii, T., Liu, Z., and Katsura, T. (2019b) A breakthrough in pressure generation by a Kawai-type multi-anvil apparatus with tungsten carbide anvils. Engineering (Beijing), 5, 434–440, https://doi.org/10.1016/j.eng.2019.01.013.

Ishii, T., Kojitani, H., and Akaogi, M. (2019c) Phase relations of Harzburgite and MORB up to the uppermost lower mantle conditions: Precise comparison with Pyrolite by multisample cell high-pressure experiments with implication to dynamics of subducted slabs. Journal of Geophysical Research. Solid Earth, 124, 3491–3507, https://doi.org/10.1029/2018JB016749.

Ishii, T., Miyajima, N., Sinmyo, R., Kojitani, H., Mori, D., Inaguma, Y., and Akaogi, M. (2020) Discovery of new structured post-spinel $MgFe_2O_4$: Crystal structure and high-pressure phase relations. Geophysical Research Letters, 47(6), e2020GL087490.

Ishii, T., Criniti, G., Bykova, E., Dubrovinsky, L., Katsura, T., Arii, H., Kojitani, H., and Akaogi, M. (2021) High-pressure syntheses and crystal structure analyses of a new low-density I_2O_4-related and $CaTi_2O_4$-type $MgAl_2O_4$ phases. American Mineralogist. Journal of Earth and Planetary Materials, 106, 1105–1112.

Ishii, T., Ohtani, E., and Shatskiy, A. (2022a) Aluminum and hydrogen partitioning between bridgmanite and high-pressure hydrous phases: Implications for water storage in the lower mantle. Earth and Planetary Science Letters, 583, 117441, https://doi.org/10.1016/j.epsl.2022.117441.

Ishii, T., Miyajima, N., Criniti, G., Hu, Q., Glazyrin, K., and Katsura, T. (2022b) High pressure-temperature phase relations of basaltic crust up to mid-mantle conditions. Earth and Planetary Science Letters, 584, 117472, https://doi.org/10.1016/j.epsl.2022.117472.

Ismailova, L., Bykova, E., Bykov, M., Cerantola, V., McCammon, C., Boffa Ballaran, T., Bobrov, A., Sinmyo, R., Dubrovinskaia, N., Glazyrin, K., and others. (2016) Stability of Fe,Al-bearing bridgmanite in the lower mantle and synthesis of pure Fe-bridgmanite. Science Advances, 2, e1600427, https://doi.org/10.1126/sciadv.1600427.

Ito, E. (2015) Multi-anvil cells and high-pressure experimental methods. In G. Schubert, Ed., Treatise on geophysics. 2nd ed., vol. 2, 233–261. Elsevier.

Kojitani, H., Katsura, T., and Akaogi, M. (2007) Aluminum substitution mechanisms in perovskite-type $MgSiO_3$: An investigation by Rietveld analysis. Physics and Chemistry of Minerals, 34, 257–267, https://doi.org/10.1007/s00269-007-0144-z.

Kubo, A. and Akaogi, M. (2000) Post-garnet transitions in the system $Mg_4Si_4O_{12}$–$Mg_3Al_2Si_3O_{12}$ up to 28 GPa: Phase relations of garnet, ilmenite and perovskite. Physics of the Earth and Planetary Interiors, 121, 85–102, https://doi.org/10.1016/S0031-9201(00)00162-X.

Lauterbach, S., McCammon, C.A., Van Aken, P., Langenhorst, F., and Seifert, F. (2000) Mössbauer and ELNES spectroscopy of (Mg, Fe)(Si, Al)O_3 perovskite: A highly oxidised component of the lower mantle. Contributions to Mineralogy and Petrology, 138, 17–26, https://doi.org/10.1007/PL00007658.

Leinenweber, K., Utsumi, W., Tsuchida, Y., Yagi, T., and Kurita, K. (1991) Unquenchable high-pressure perovskite polymorphs of $MnSnO_3$ and $FeTiO_3$. Physics and Chemistry of Minerals, 18, 244–250, https://doi.org/10.1007/BF00202576.

Liu, Z., Ishii, T., and Katsura, T. (2017a) Rapid decrease of $MgAlO_{2.5}$ component in bridgmanite with pressure. Geochemical Perspectives Letters, 5, 12–18, https://doi.org/10.7185/geochemlet.1739.

Liu, Z., Nishi, M., Ishii, T., Fei, H., Miyajima, N., Boffa Ballaran, T., Ohfuji, H., Sakai, T., Wang, L., Shcheka, S., and others. (2017b) Phase relations in the system $MgSiO_3$-Al_2O_3 up to 2300 K at lower mantle pressures. Journal of Geophysical Research. Solid Earth, 122, 7775–7788, https://doi.org/10.1002/2017JB014579.

Liu, Z., McCammon, C., Wang, B., Dubrovinsky, L., Ishii, T., Bondar, D., Nakajima, A., Tange, Y., Higo, Y., Cui, T., and others. (2020) Stability and solubility of the $FeAlO_3$ component in bridgmanite at uppermost lower mantle conditions. Journal of Geophysical Research. Solid Earth, 125, e2019JB018447, https://doi.org/10.1029/2019JB018447.

McCammon, C.A. (1994) A Mössbauer milliprobe: Practical considerations. Hyperfine Interactions, 92, 1235–1239, https://doi.org/10.1007/BF02065761.

McCammon, C.A., Chaskar, V., and Richards, G.G. (1991) A technique for spatially resolved Mossbauer spectroscopy applied to quenched metallurgical slags. Measurement Science & Technology, 2, 657, https://doi.org/10.1088/0957-0233/2/7/014.

McCammon, C., Hutchison, M., and Harris, J. (1997) Ferric iron content of mineral inclusions in diamonds from Sao Luiz: A view into the lower mantle. Science, 278, 434–436, https://doi.org/10.1126/science.278.5337.434.

McCammon, C.A., Lauterbach, S., Seifert, F., Langenhorst, F., and Van Aken, P.A. (2004) Iron oxidation state in lower mantle mineral assemblages: I. Empirical relations derived from high-pressure experiments. Earth and Planetary Science Letters, 222, 435–449, https://doi.org/10.1016/j.epsl.2004.03.018.

Navrotsky, A. (1999) A lesson from ceramics. Science, 284, 1788–1789, https://doi.org/10.1126/science.284.5421.1788.

Navrotsky, A., Schoenitz, M., Kojitani, H., Xu, H., Zhang, J., Weidner, D.J., and Jeanloz, R. (2003) Aluminum in magnesium silicate perovskite: Formation, structure, and energetics of magnesium-rich defect solid solutions. Journal of Geophysical Research. Solid Earth, 108, (B7), https://doi.org/10.1029/2002JB002055.

Ono, S., Ito, E., and Katsura, T. (2001) Mineralogy of subducted basaltic crust (MORB) from 25 to 37 GPa, and chemical heterogeneity of the lower mantle. Earth and Planetary Science Letters, 190, 57–63, https://doi.org/10.1016/S0012-821X(01)00375-2.

Prescher, C., McCammon, C., and Dubrovinsky, L. (2012) MossA: A program for analyzing energy-domain Mössbauer spectra from conventional and synchrotron sources. Journal of Applied Crystallography, 45, 329–331, https://doi.org/10.1107/S0021889812004979.

Reali, R., Van Orman, J.A., Pigott, J.S., Jackson, J.M., Boioli, F., Carrez, P., and Cordier, P. (2019) The role of diffusion-driven pure climb creep on the rheology of bridgmanite under lower mantle conditions. Scientific Reports, 9, 2053, https://doi.org/10.1038/s41598-018-38449-8.

Uenver-Thiele, L., Woodland, A.B., Miyajima, N., Boffa Ballaran, T., and Frost, D.J. (2018) Behaviour of Fe_4O_5-$Mg_2Fe_2O_5$ solid solutions and their relation to coexisting Mg-Fe silicates and oxide phases. Contributions to Mineralogy and Petrology, 173, 20, https://doi.org/10.1007/s00410-018-1443-8.

White, R.S. and McKenzie, D. (1995) Mantle plumes and flood basalts. Journal of Geophysical Research, 100 (B9), 17543–17585, https://doi.org/10.1029/95JB01585.

Yoshino, T., Kamada, S., Zhao, C., Ohtani, E., and Hirao, N. (2016) Electrical conductivity model of Al-bearing bridgmanite with implications for the electrical structure of the Earth's lower mantle. Earth and Planetary Science Letters, 434, 208–219, https://doi.org/10.1016/j.epsl.2015.11.032.

Manuscript received January 18, 2022
Manuscript accepted April 27, 2022
Accepted manuscript online May 5, 2022
Manuscript handled by Susannah Dorfman